Strong unidirectional Rashba state induced by extended vacancy line defects in a $1T'$-WTe$_2$ monolayer

Moh. Adhib Ulil Absor ,[*] Iman Santoso , and Harsojo

Department of Physics, Faculty of Mathematics and Natural Sciences, Universitas Gadjah Mada,
Sekip Utara BLS 21, Yogyakarta 55186, Indonesia

The correlation between spin-orbit coupling and low crystal symmetry in the $1T'$ phase of the tungsten ditellurides (WTe$_2$) monolayer (ML) plays a significant role in its electronic and topological properties. However, the centrosymmetric nature of the crystal maintains Kramer's spin degeneracy in its electronic states, which limits its functionality in spintronics. In this paper, through a systematic study using first-principles calculations, we show that significant spin splitting can be induced in the $1T'$-WTe$_2$ ML by introducing a one-dimensional (1D) vacancy line defect (VLD). We examine six configurations of the 1D VLD, which consist of three VLDs extended in the armchair direction including a Te$_1$ armchair-VLD (ACV_{Te_1}), Te$_2$ armchair-VLD (ACV_{Te_2}), and W armchair-VLD (ACV_W), and three VLDs elongated along the zigzag direction comprising a Te$_1$ zigzag-VLD (ZZV_{Te_1}), Te$_2$ zigzag-VLD (ZZV_{Te_2}), and W zigzag-VLD (ZZV_W), where Te$_1$ and Te$_2$ are two nonequivalent Te atoms located at the lower and higher sites in the top layer, respectively. We find that both the ACV_{Te_1} and ACV_W systems have the lowest formation energy. Concerning these two most stable VLD systems, we identify large spin splitting in the defect states near the Fermi level driven by a strong coupling of the in-plane $p - d$ orbitals, displaying highly unidirectional Rashba states with perfectly collinear spin configurations in the momentum space. This unique spin configuration gives rise to a specific spin mode that protects the spin from decoherence and leads to an exceptionally long spin lifetime. Furthermore, the observed unidirectional Rashba states are enforced by the inversion symmetry breaking and the 1D nature of the VLD, as clarified by the $\vec{k} \cdot \vec{p}$ model derived from the symmetry analysis. Our findings pave a possible way to induce significant spin splitting in the $1T'$-WTe$_2$ ML, which could be highly important for designing highly efficient spintronic devices.

I. INTRODUCTION

Two-dimensional (2D) layered materials arranged through van der Waals forces have attracted substantial interest for recent years due to their fascinating characteristics and immense promise across (opto)electronics [1–3] and spintronics [4], as well as energy conversion [5,6]. Among these 2D layered materials, transition metal dichalcogenides (TMDCs) hold a notable portion [7], featuring a range of MX_2 compositions where M stands for a transition metal element and X represents a chalcogen element. Weak van der Waals interactions between successive MX_2 layers permit the separation of TMDCs into single layers through the method of mechanical exfoliation [8]. The common bulk phases of the TMDCs include $2H$, $1T$, and $3R$ phases involving stacking layers with hexagonal, octahedral, and rhombohedral symmetries, respectively [7,9,10]. While $2H$ and $3R$ phases exhibit trigonal prismatic coordination of metal atoms, the $1T$ phase has trigonal antiprismatic or octahedral coordination. Moreover, the metastable $1T$ phase tends to spontaneously distort its lattice by dimerizing transition metal atoms along one direction, leading to reduced lattice symmetry. This structure features one-dimensional dimers of metal atoms flanked by zigzag chains of chalcogen atoms, exhibiting an inversion-symmetric $1T'$ and an inversion symmetry-broken T_d stacking order [11–13]. In the monolayer (ML) limit, even though the stable $1H$ and $1T$ phases are present, the $1T'$ and T_d phases also emerge, depending on the specific pairing of transition metal M and chalcogen X elements [11–13]. The diverse combinations of chemical compositions and structural phases in TMDCs ML lead to a wide spectrum of electronic properties, which encompasses variations in band structure character (metallic or insulating) [7,14] and the emergence of correlated and topological phases [11,14,15]. This underscores the suitability of TMDCs ML as an excellent platform for future-generation technologies.

An important characteristic discovered within TMDCs ML pertains to the robust influence of spin-orbit coupling (SOC), prominently observed in the $1H$ phase, as seen in molybdenum and tungsten dichalcogenides [16–21]. In this context, the absence of inversion symmetry in the crystal arrangement, coupled with the strong SOC exhibited by the $5d$ orbitals of the transition metal atoms, gives rise to a significant spin splitting within the electronic band structures. This spin splitting is believed to underlie intriguing phenomena in the TMDCs ML, including the spin Hall effect [11,22], selective spin-dependent rules for optical transitions [23], and the

*Corresponding author: adib@ugm.ac.id

magnetoelectric effect [24]. Additionally, owing to the in-plane mirror symmetry present in the crystal structures of TMDCs ML, a distinctive out-of-plane spin polarization is retained within the spin-split bands surrounding the K point within the first Brillouin zone (FBZ), resulting in a Zeeman-type spin splitting [16–18,21]. This phenomenon is projected to display substantial spin coherence and prolonged spin relaxation for electrons [21]. Furthermore, recent reports highlight the feasibility of electrically manipulating spin splitting and spin polarization in the TMDCs ML, rendering them well suited for applications in spintronics devices like spin-field effect transistors (SFET) [25].

In comparison to the $1H$ phase of TMDCs ML, the influence of the SOC in the $1T'$ phases presents an equally captivating aspect. Particularly, the ML form of tungsten ditellurides (WTe$_2$) in the $1T'$ structure has garnered considerable scientific interest following its successful synthesis [14,15,26–30]. This ML embodies a complex interplay between the arrangement of bands linked to the SOC and the characteristics of W d-orbitals, which shed light on electronic correlations [14,15,26,27,31–35]. Recent theoretical predictions [33,34] and experimental observations [29] have unveiled the emergence of a canted quantum spin Hall effect within the WTe$_2$ ML, driven by a canted unidirectional SOC. This discovery adds a new dimension to the potential utilization of topological materials in spintronic applications [34,35]. In addition, the interplay of the SOC, low crystal symmetry, and high electron mobilities give rise to other phenomena of interest such as large spin-orbit torques [6,36] that could be used in spintronic devices. However, it is worth noting that, in the $1T'$ phase of the WTe$_2$ ML, the electronic band structures maintain spin degeneracy due to the crystal's centrosymmetric nature, which imposes limitations on its functionality in spintronics. Given the WTe$_2$ ML's remarkable transport properties [15,26,27,29–31,33–35], the key to enabling its use in spintronic devices likely lies in overcoming this spin degeneracy. Thus identifying a viable approach to induce substantial spin splitting within the $1T'$ phase of WTe$_2$ ML becomes a highly desirable pursuit.

In this paper, by using density-functional theory (DFT) calculations, we report that significant spin splitting can be induced in the $1T'$-WTe$_2$ ML by introducing one-dimensional (1D) extended vacancy line defect (VLD). Previous research has already highlighted the significant impact of surface imperfections on the electronic and topological properties of the $1T'$-WTe$_2$ ML such as point defects [37–40] and 1D edge step surfaces [41,42]. Since the emergence of the vacancy defects in the $1T'$-WTe$_2$ ML has been experimentally reported through a scanning tunneling microscopy study [41], this suggests that realization of the VLD in the $1T'$-WTe$_2$ ML is highly plausible. In our study, we consider six configurations of the 1D VLD, which consist of three VLDs extended in the armchair direction and three VLDs elongated along the zigzag direction. The armchair-VLDs include a Te$_1$ armchair-VLD (ACV_{Te_1}), Te$_2$ armchair-VLD (ACV_{Te_2}), and W armchair-VLD (ACV_W), while the zigzag-VLDs comprise a Te$_1$ zigzag-VLD (ZZV_{Te_1}), Te$_2$ zigzag-VLD (ZZV_{Te_2}), and W zigzag-VLD (ZZV_W), where Te$_1$ and Te$_2$ are two nonequivalent Te atoms located at the lower and higher sites in the top layer, respectively. Our findings reveal that both the ACV_{Te_1}

and ACV_W have the lowest formation energy. By focusing on these two most stable VLDs, we observe a significant spin splitting in the defect states near the Fermi level imposed by a strong hybridization of the in-plane $p - d$ orbitals, exhibiting highly unidirectional Rashba states with perfectly collinear spin configurations in the momentum space. These particular spin configurations result in a specific spin mode that protects the spin from decoherence and results in an extremely long spin lifetime [43–47]. Furthermore, the observed unidirectional Rashba states are enforced by the inversion symmetry breaking and the 1D nature of the defect, as confirmed by the $\vec{k} \cdot \vec{p}$ model derived from the symmetry analysis. Finally, a possible application of the present system for spintronics will be discussed.

II. COMPUTATIONAL DETAILS

All DFT calculations were performed based on norm-conserving pseudopotentials and optimized pseudoatomic localized basis functions implemented in the OPENMX code [48–50]. The exchange-correlation function was treated within generalized gradient approximation by Perdew, Burke, and Ernzerhof (GGA-PBE) [51,52]. The basis functions were expanded by a linear combination of multiple pseudoatomic orbitals (PAOs) generated using a confinement scheme [48,49], where three s-, three p-, and two d-character numerical PAOs were used. The accuracy of the basis functions, as well as pseudopotentials we used, were carefully benchmarked by the delta gauge method [53].

To simulate the VLD, we constructed a supercell of the pristine $1T'$-WTe$_2$ ML by using the optimized primitive rectangular unit cell [Figs. 1(a) and 1(b)]. Here, we used the axis system where the $1T'$-WTe$_2$ ML is chosen to sit on the $x - y$ plan, where the x (y) axis was oriented parallel to the zigzag (armchair) direction. We explore six distinct configurations of the 1D VLD, comprising three VLDs extended in the armchair direction and three in the zigzag direction. Specifically, for the armchair-oriented 1D VLD, we examine three configurations, namely a Te$_1$ armchair-VLD (ACV_{Te_1}), Te$_2$ armchair-VLD (ACV_{Te_2}), and W armchair-VLD (ACV_W), as depicted in Figs. 1(c)–1(e), respectively. Conversely, in the case of the 1D VLD elongated along the zigzag direction, we analyze three configurations, including a Te$_1$ zigzag-VLD (ZZV_{Te_1}), Te$_2$ zigzag-VLD (ZZV_{Te_2}), and W zigzag-VLD (ZZV_W) as shown in Figs. 1(f)–1(h), respectively. Here, Te$_1$ and Te$_2$ are the Te atoms which are distinguished by their position in the lower and higher sites in the top layer of the $1T'$-WTe$_2$ ML, as shown in Fig. 1(b). The first Brillouin zone (FBZ) for the primitive unit cell and the corresponding supercell of the VLD systems is shown in Fig. 1(i). To represent these VLDs in our simulations, we enlarged the supercell size by a factor of 7 in the zigzag (x) and armchair (y) direction for the armchair-VLD and zigzag-VLD systems, respectively, to prevent interactions between periodic images of the line defects [see Figs. 1(c)–1(h)]. We used a periodic slab with a sufficiently large vacuum layer (20 Å) to avoid interaction between adjacent layers. The $2 \times 8 \times 1$ k-point and $12 \times 2 \times 1$ k-point meshes were used for the armchair-VLD and zigzag-VLD systems, respectively. The geometries were
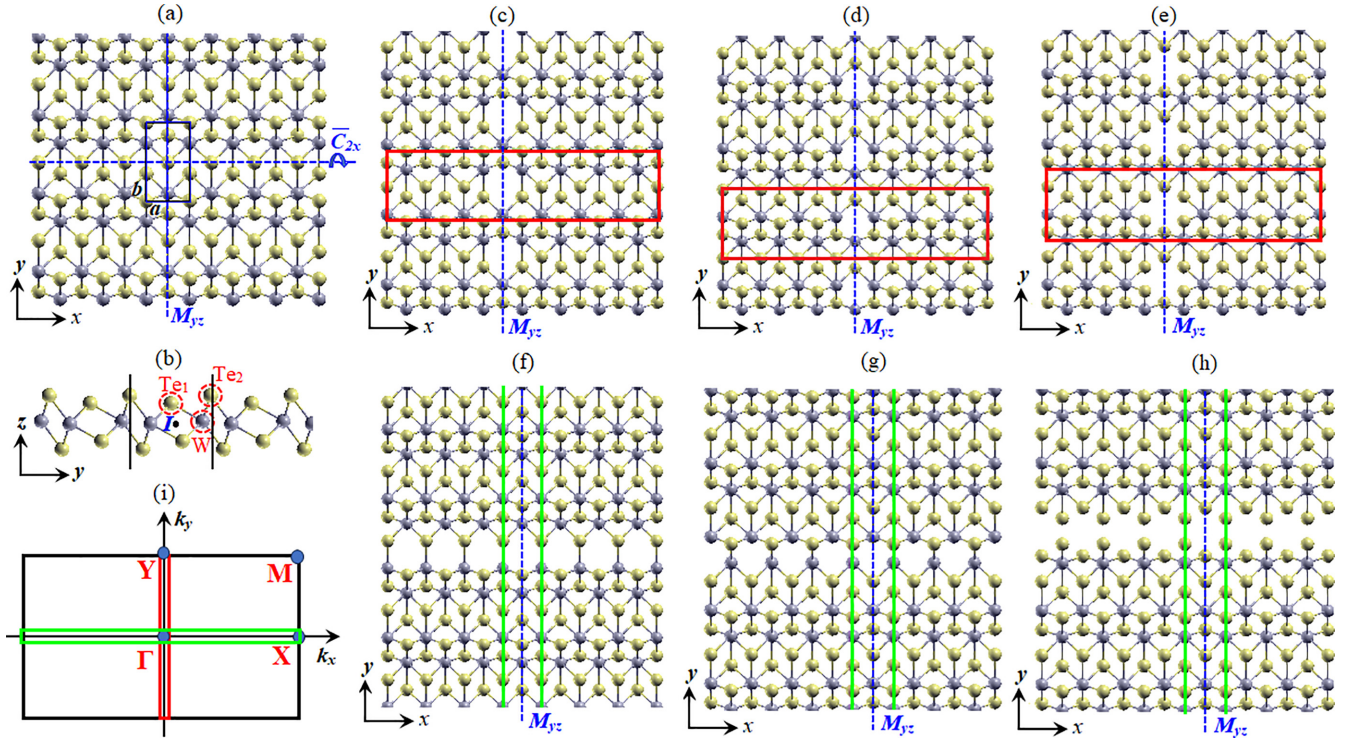
FIG. 1. (a),(b) Top and side views of the pristine $1T'$-WTe$_2$ ML is shown, respectively. The black line represents the primitive rectangular unit cell with a and b lattice parameters along the x and y direction, respectively. Here, two nonequivalent Te sites (Te$_1$ and Te$_2$) distinguished by the lower and higher sites in the top layer of the $1T'$-WTe$_2$ ML, respectively, are indicated. Top and side views for the 1D VLD supercell with (c) a Te$_1$ armchair-VLD (ACV_{Te_1}), (d) a Te$_2$ armchair-VLD (ACV_{Te_2}), (e) a W armchair-VLD (ACV_W), (f) a Te$_1$ zigzag-VLD (ZZV_{Te_1}), (g) a Te$_2$ zigzag-VLD (ZZV_{Te_2}), and (h) a W zigzag-VLD (ZZV_W) configurations are shown. The red and green rectangles indicate the 1D supercell with the VLD extended along the armchair and zigzag directions, respectively. (i) The FBZ of the primitive rectangular unit cell and the corresponding 1D armchair-VLD (red lines) and zigzag-VLD (green lines) supercells are shown. The symmetry operations including inversion symmetry (I), a mirror symmetry (M_{yz}) perpendicular to the x axis, and a twofold screw rotation symmetry ($\bar{C}_{2x}$) around the x axis are indicated.

fully relaxed until the force acting on each atom was less than 1 meV/Å.

To confirm the energetic stability of the VLD, we compute the formation energy E^f through the following formula [54,55]:

$$E^f = E_{VLD} - E_{pristine} + \sum_i n_i \mu_i. \tag{1}$$

In Eq. (1), E_{VLD} is the total energy of the VLD system, $E_{pristine}$ is the total energy of the pristine $1T'$ WTe$_2$ ML supercell, n_i is the number of atoms being removed from the pristine system, and μ_i is the chemical potential of the removed atoms corresponding to the chemical environment surrounding the system. Here, μ_i obtains the following requirements:

$$E_{WTe_2} - 2E_{Te} \leqslant \mu_W \leqslant E_W, \tag{2}$$

$$\tfrac{1}{2}\left(E_{WTe_2} - E_W\right) \leqslant \mu_{Te} \leqslant E_{Te}. \tag{3}$$

Under the Te-rich condition, μ_{Te} is the energy of the Te atom in the bulk phase which corresponds to the lower limit on W, $\mu_W = E_{WTe_2} - 2E_{Te}$, where E_{WTe_2} is the total energy of the $1T'$-WTe$_2$ ML in the primitive unit cell. On the other hand, in the case of the W-rich condition, μ_W is associated with the

energy of the W atom in the bulk phase corresponding to the lower limit on Te, $\mu_{Te} = \frac{1}{2}(E_{WTe_2} - E_W)$.

To evaluate electronic properties of the pristine and defective $1T'$-WTe$_2$ ML, we calculate band structures corresponding to the orbital-resolved projected bands along the specific k path of the FBZ as depicted in Fig. 1(i). We then calculate spin-resolved projected bands by evaluating the spin vector component (S_x, S_y, S_z) in the k space by using the spin density matrix after a self-consistent field is achieved in the DFT calculations [56]. The spin density matrix, denoted as $P_{\sigma\sigma'}(\vec{k}, \mu)$, is computed using the spinor Bloch wave function, $\Psi_\mu^\sigma(\vec{r}, \vec{k})$, through the following equation:

$$P_{\sigma\sigma'}(\vec{k}, \mu) = \int \Psi_\mu^\sigma(\vec{r}, \vec{k}) \Psi_\mu^{\sigma'}(\vec{r}, \vec{k}) d\vec{r}$$

$$= \sum_n \sum_{i,j} [c_{\sigma\mu i}^* c_{\sigma'\mu j} S_{i,j}] e^{\vec{R}_n \cdot \vec{k}}, \tag{4}$$

where $\Psi_\mu^\sigma(\vec{r}, \vec{k})$ is obtained after self-consistency is achieved in the DFT calculation. In Eq. (1), S_{ij} is the overlap integral of the ith and jth localized orbitals, $c_{\sigma\mu i(j)}$ is the expansion coefficient, σ (σ') is the spin index ($\uparrow$ or $\downarrow$), μ is the band index, and $\vec{R}_n$ is the nth lattice vector.
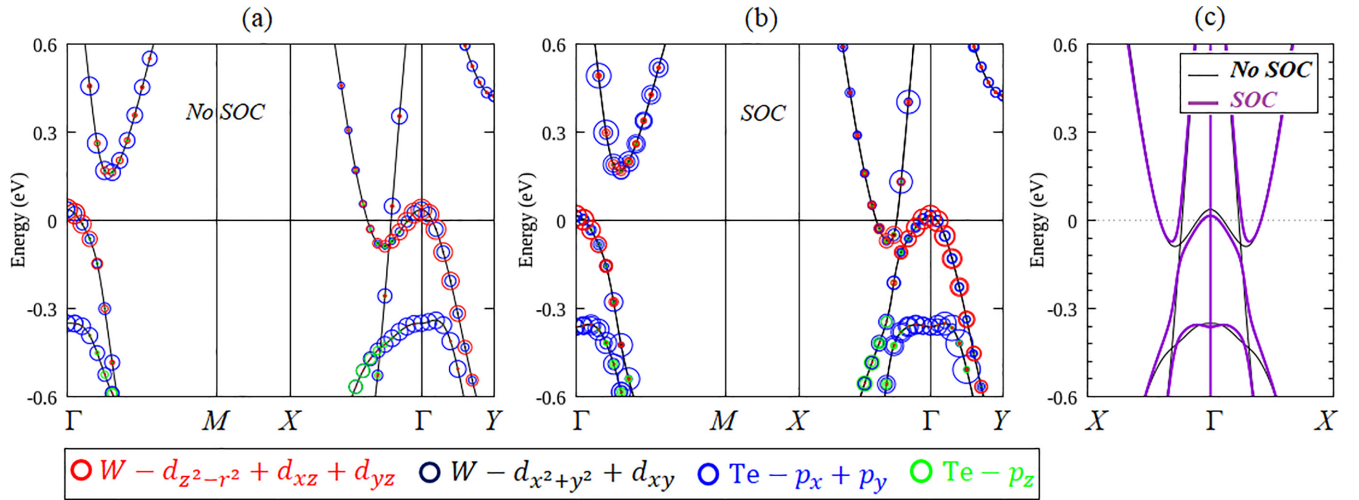
FIG. 2. (a),(b) Orbital resolved of the electronic band structure of the pristine (1×1) $1T'$-WTe$_2$ ML calculated without and with the spin-orbit coupling (SOC), respectively. The orbital atomic components are indicated by the color circles, where the radii of the circles reflect the magnitude of the spectral weight of the particular orbitals to the bands. (c) Band dispersion of the pristine (1×1) $1T'$-WTe$_2$ ML along the $X - \Gamma - X$ line calculated with (red lines) and without (black lines) the SOC is highlighted.

III. RESULT AND DISCUSSION

Before examining the defective systems, we first provide a brief overview of the structural symmetry and electronic properties of the pristine system. The ML structure of WTe$_2$ adopts a stable $1T'$ structure, in which the W atoms are organized in octahedral coordination with the Te atoms. This arrangement leads to a slightly buckled zigzag chain of W atoms due to metallic bonding, resulting in a distortion of the Te octahedron around each Te atom [Figs. 1(a) and 1(b)]. The crystal structure of the $1T'$-WTe$_2$ ML is centrosymmetric and its symmetry belongs to the C_{2h} point group, characterized by several symmetry operations including identity (E), inversion symmetry (I), a mirror symmetry (M_{yz}) perpendicular to the x axis, and a twofold screw rotation symmetry ($\bar{C}_{2x}$) around the x axis, as displayed in Figs. 1(a) and 1(b). The optimized lattice parameters a and b of the $1T'$-WTe$_2$ ML are found to be 3.51 Å and 6.23 Å, respectively. Nevertheless, these results are consistent with previous theoretical reports [26,37,57,58] and experimental data [26–28]. Notably, the substantial difference between the a and b parameters signifies pronounced anisotropy in the crystal geometry, implying that this material exhibits highly anisotropic electronic, mechanical, and optical properties when subjected to uniaxial strain along the x and y directions [57,58].

Figures 2(a) and 2(b) show the orbital-resolved electronic band structure of the pristine (1×1) $1T'$-WTe$_2$ ML along the selected $\vec{k}$ path in the FBZ calculated with and without the SOC, respectively, while Fig. 2(c) highlights the band dispersion near the Fermi level along the $X - \Gamma - X$ line. In the absence of the SOC, one can see that the $1T'$-WTe$_2$ ML shows a semimetallic character of the electronic states, exhibiting Dirac crossing bands between the highest occupied state (HOS) and lowest unoccupied state (LUS) at the k point along the $X - \Gamma$ line near the Fermi level [Figs. 2(a) and 2(c)]. These crossing bands are protected by $\bar{C}_{2x}$ screw rotation as well as I inversion symmetries of the C_{2h} point group. Due to the close electronegativity between the W and Te atoms, the

W-$d_{z^2-r^2} + d_{xz} + d_{yz}$ states are strongly hybridized with the Te-$p_x + p_y$ states around the Fermi level [Fig. 2(b)], which is in contrast to the widely studied $1H$-MX_2 TMDCs ML, where the band gap occurs between the occupied transition metal $M - d$ and unoccupied chalcogen $X - p$ states [16–21]. With the inclusion of SOC, the bands further hybridize with each other due to the strong mixing between W-$d_{z^2-r^2} + d_{xz} + d_{yz}$ and Te-$p_x + p_y$ states and the degeneracies at the Dirac crossing points are lifted [Figs. 2(b) and 2(c)]. Accordingly, opening a band gap in the bulk states occurs; thus the $1T'$-WTe$_2$ ML becomes a 2D topological insulator [14,15,31–35]. However, due to the presence of the inversion symmetry in the $1T'$-WTe$_2$ ML, all the bands remain degenerated in the entirely FBZ [see Figs. 2(b) and 2(c)].

We emphasized here that the absence of the spin-splitting bands plays a detrimental role in the spintronic properties of the $1T'$-WTe$_2$ ML. Therefore, we applied the 1D VLD to break the inversion symmetry of the $1T'$-WTe$_2$ ML, which is expected to induce the substantial spin-splitting bands. In fact, the defect inducing large band splitting has been previously reported on the $1H$ and $1T$ types of the TMDCs MLs [55,59–62].

Next, we consider the effect of the VLD on the structural symmetry and electronic properties of the $1T'$-WTe$_2$ ML. We first examine the optimized structure of the VLD systems by evaluating the W-Te$_1$ and W-Te$_2$ bond lengths (d_{W-Te_1}, d_{W-Te_2}) near the VLD site, as presented in Table I. Generally, due to the atomic relaxation during the structural optimization, the position of the atoms near the VLD site is sensitively displaced from that of the pristine system [55,59]. In the case of the armchair-VLD systems, the formation of the ACV_{Te_1} breaks the inversion I and twofolds screw rotation $\bar{C}_{2x}$ symmetries [Fig. 1(c)]. Here, removing a Te atom at the Te$_1$ site leads to the relaxation of the three W atoms surrounding the VLD site, resulting in the d_{W-Te_1} (2.73 Å) being smaller than that for the pristine system ($d_{W-Te_1} = 2.74$ Å). However, the d_{W-Te_2} (2.85 Å) is larger than that of the pristine one ($d_{W-Te_1} = 2.83$ Å). As a result, only a mirror symmetry plane

TABLE I. Calculated formation energy (measured in eV) of the Te-rich ($E^f_{\text{Te-rich}}$) and W-rich ($E^f_{\text{W-rich}}$) for the VLD systems corresponding to the W-Te$_1$ bond length ($d_{\text{W}-\text{Te}_1}$, in Å) and the W-Te$_2$ bond length ($d_{\text{W}-\text{Te2}}$, in Å) around the VLD site compared with that of the pristine systems. We also provide the calculated results of the single vacancy defect (SVD), such as Te$_1$ SVD ($V^{\text{SVD}}_{\text{Te}_1}$), Te$_2$ SVD ($V^{\text{SVD}}_{\text{Te}_2}$), and W SVD ($V^{\text{SVD}}_{\text{W}}$), and compare these results with those obtained from the previous reports for a comparison.

Defective systems	$(E^f_{\text{Te-rich}}; E^f_{\text{We-rich}})$ (eV)	$d_{\text{W}-\text{Te}_1}$ (Å)	$d_{\text{W}-\text{Te}_2}$ (Å)	Reference
Pristine		2.74	2.84	This work
		2.72	2.82	Ref. [37]
Vacancy line defect (VLD)				
Armchair-VLD				
ACV_{Te_1}	(2.37; 2.53)	2.73	2.85	This work
ACV_{Te_2}	(2.86; 3.06)	2.76	2.91	This work
ACV_{W}	(1.97; 2.46)	2.66	2.84	This work
Zigzag-VLD				
ZZV_{Te_1}	(2.95; 3.26)	2.76	2.84	This work
ZZV_{Te_2}	(3.02; 3.32)	2.78	2.86	This work
ZZV_{W}	(2.72; 2.93)	2.71	2.88	This work
Single vacancy defect (SVD)				
$V^{\text{SVD}}_{\text{Te}_1}$	(2.31; 2.42)	2.72	2.83	This work
	(2.37; 2.53)			Ref. [37]
	2.21			Ref. [38]
$V^{\text{SVD}}_{\text{Te}_2}$	(2.52; 2.72)	2.76	2.87	This work
	(2.53; 2.70)			Ref. [37]
$V^{\text{SVD}}_{\text{W}}$	(1.59; 2.35)	2.67	2.85	This work

(M_{yz}) along the extended vacancy line remains [Fig. 1(c)], leading to the fact that the symmetry of the ACV_{Te_1} system belongs to the C_s point group. This point group symmetry is also retained for other armchair-VLD systems (ACV_{Te_2} and ACV_{W}) as depicted on Figs. 1(d) and 1(e). However, the different atomic missing in both the ACV_{Te_2} and ACV_{W} leads to distinct effects on the W-Te bond length near the VLD site. For example, in the case of the ACV_{Te_2} system, the absence of the Te atom at the Te$_2$ site results in both $d_{\text{W}-\text{Te}_1}$ (2.76 Å) and $d_{\text{W}-\text{Te}_2}$ (2.91 Å) being considerably larger than those observed in the $ACV\text{Te}_1$ and pristine systems. Conversely, the missing of a W atom in the formation of ACV_{W} significantly reduces $d_{\text{W}-\text{Te}_1}$ (2.66 Å), while slightly increasing $d_{\text{W}-\text{Te}_2}$ (2.84 Å).

Similarly, the optimized structure of the zigzag-VLD systems also undergoes significant atomic relaxation and distortion in comparison to the pristine system as shown in Figs. 1(f)–1(h). The absence of a Te atom at the Te$_2$ site leads to the formation of ZZV_{Te_2} [Fig. 1(g)]. Here, the optimized atomic structure yields the bond lengths $d_{\text{W}-\text{Te}_1}$ and $d_{\text{W}-\text{Te}_2}$ measuring 2.78 Å and 2.86 Å, respectively, near the VLD site, which is notably larger than those observed in the pristine system. A similar atomic relaxation is also observed in the ZZV_{Te_1} system [Fig. 1(f)], in which the missing of the Te atom at the Te$_1$ site results in the substantial W-Te bond lengths ($d_{\text{W}-\text{Te}_1}$ = 2.76 Å, $d_{\text{W}-\text{Te}_2}$ = 2.84 Å), which are slightly smaller than those in the ZZV_{Te_2} system. The smaller W-Te bond lengths ($d_{\text{W}-\text{Te}_1}$, $d_{\text{W}-\text{Te}_2}$) in the ZZV_{Te_1} system compared to the ZZV_{Te_2} system are consistent with those observed on the Te-based armchair VLD systems. However, resembling the structural distortion seen in the ACV_{W} system, the formation of the ZZV_{W} induces the relaxation of the Te atoms near the VLD sites [Fig. 1(h)], which is stabilized by a reduction in $d_{\text{W}-\text{Te}_1}$ (2.71 Å) and an increase in $d_{\text{W}-\text{Te}_2}$

(2.88 Å). It is noteworthy that all zigzag-VLD systems display a C_s point group symmetry due to the presence of a single mirror symmetry plane (M_{yz}) perpendicular to the extended vacancy line [refer to Figs. 1(f)–1(h)].

The structural modification induced by the presence of the VLDs significantly influenced the energetic stability of the $1T'$-WTe$_2$ ML, which can be confirmed by computing the formation energy E_f. As shown in Table I, we find that both the $ACV_{\text{Te}1}$ and ACV_{W} systems have the lowest E_f in both the Te-rich and W-rich formations, indicating that these systems are the most favorable VLDs to be formed in $1T'$-WTe$_2$ ML. In addition, for both the armchair and zigzag VLD systems, we observed that the E_f of the W-based VLD systems is lower than that of the Te-based VLD systems (see Table I), which is in contrast to the widely studied defective systems observed on the $1H$ and $1T$ phase of the TMDCs ML. For instance, the single chalcogen vacancies and their alignment into the extended line defect have been reported to exhibit the lowest E_f as recently predicted on $1H$-MoS$_2$ ML [59,63,64] and $1H$-WS$_2$ [59,61], and $1T$-PtSe$_2$ [55,59,60,65]. To further analyze the stability of the VLD systems, we also compare the calculated E_f of the VLD with those of the single vacancy defect (SVD) systems such as Te$_1$ SVD ($V^{\text{SVD}}_{\text{Te}_1}$), Te$_2$ SVD ($V^{\text{SVD}}_{\text{Te}_2}$), and W SVD ($V^{\text{SVD}}_{\text{W}}$), as presented in Table I. Consistent with the VLD systems, we revealed that the E_f of the $V^{\text{SVD}}_{\text{W}}$ is lower than that of the Te-based SVDs ($V^{\text{SVD}}_{\text{Te}_1}$, $V^{\text{SVD}}_{\text{Te}_2}$). The lower E_f of the $V^{\text{SVD}}_{\text{W}}$ system compared with that of the Te-based SVD systems is also in agreement with previous results of the SVD systems observed in the bulk $1T'$ WTe$_2$ as reported by Ref. [39].

Figures 3(a)–3(c) shows the electronic band structures of armchair-VLD systems calculated without and with the SOC, showcasing orbital-resolved bands projected onto atoms near
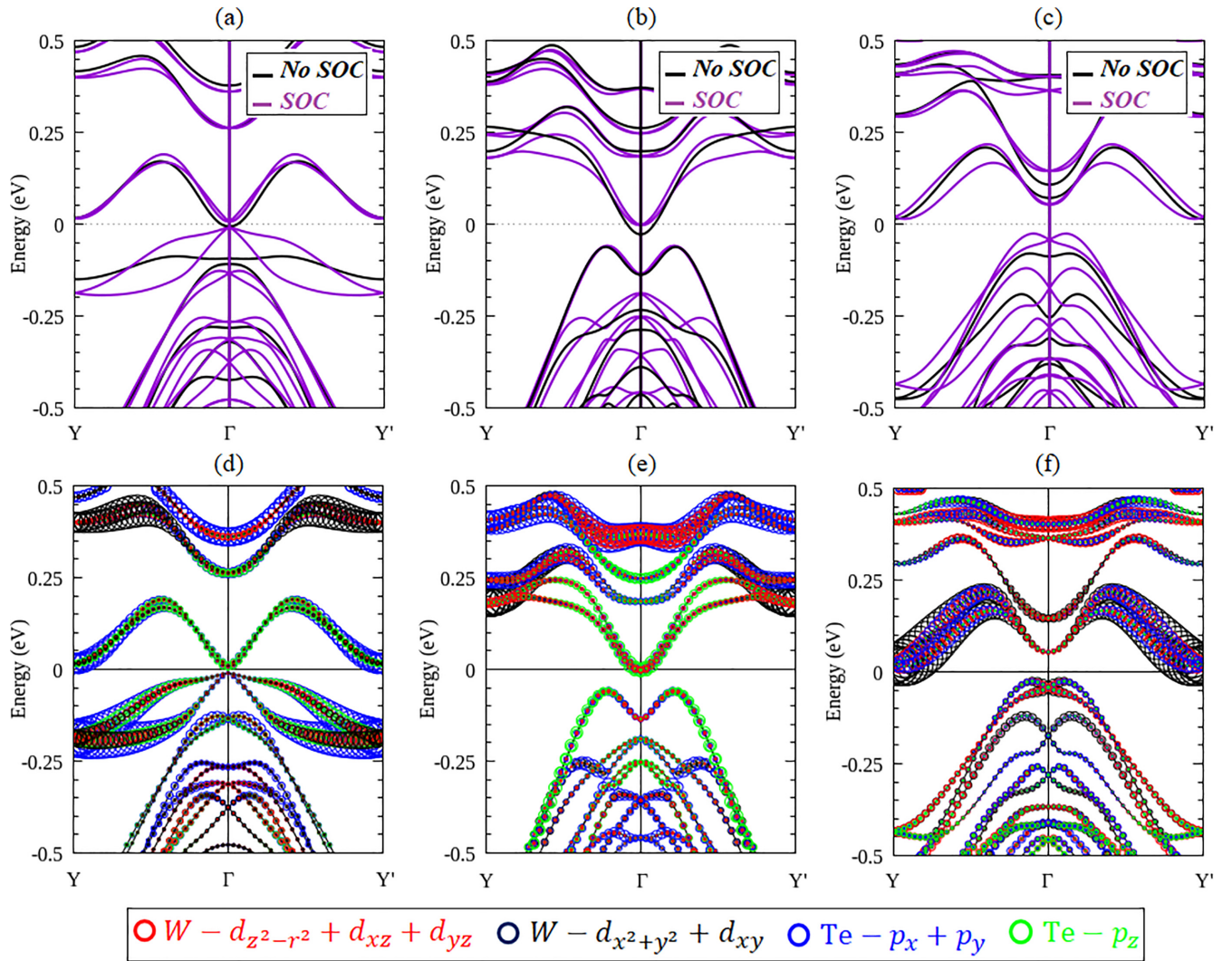
FIG. 3. Electronic structures of the armchair-VLD systems. Electronic band structures calculated without (black lines) and with (red lines) the SOC for (a) ACV_{Te_1}, (b) ACV_{Te_2}, and (c) ACV_W systems are shown. Orbital-resolved projected bands calculated for (d) ACV_{Te_1}, (e) ACV_{Te_2}, and (f) ACV_W (g)–(i) systems are presented by the color circle, where the radii of the circles reflect the magnitude of the spectral weight of the particular orbitals to the bands.

the VLD site [Figs. 3(d)–3(f)]. Without the SOC, both the ACV_{Te_1} and ACV_{Te_2} systems exhibit metallic behavior, as evident from the crossing of the LUS to the Fermi level near the Γ point [Figs. 3(a) and 3(b)]. However, in both systems, the HOS lies notably below the Fermi level along the Γ − Y line, resulting in an energy gap between the LUS and HOS [Figs. 3(a) and 3(b)]. This gap is measured to be 0.1 eV and 0.04 eV for the ACV_{Te_1} and ACV_{Te_2} systems, respectively. Upon considering the SOC, elevated energy levels of both the LUS and HOS around the Γ point occur owing to strong hybridization between the W-$d_{z^2-r^2} + d_{xz} + d_{yz}$ and Te-p_z orbitals [see Figs. 3(d) and 3(e)]. Consequently, both the ACV_{Te_1} and ACV_{Te_2} systems undergo a transition into semiconductors with small band gaps of 0.025 eV and 0.07 eV, respectively. This shift from metallic to semiconductor states, influenced by the hybridization of the out-of-plane $p − d$ orbitals, aligns with previous reports on Te-based SVD systems on the $1T'$ WTe$_2$ ML [37,38]. On the other hand, the ACV_W system behaves as a semiconductor with a substantial indirect band gap of 0.11 eV,

where the LUS and HOS reside at the Y and Γ points, respectively [see Fig. 3(c)]. This band gap reduces to 0.075 eV when considering the SOC, attributed to the coupling between the W-$d_{x^2+y^2} + d_{xy}$ and Te-$p_x + p_y$ orbitals in the LUS around the X point and coupling between the W-$d_{z^2-r^2} + d_{xz} + d_{yz}$ and Te-p_z orbitals in the HOS around the Γ point [see Fig. 3(f)]. In contrast to the armchair-VLD systems, all the zigzag-VLD systems exhibit a metallic state [Figs. 4(a)–4(c)]. Our orbital projection analysis indeed confirmed that the electronic states near the Fermi level are dominantly characterized by the mixing of the W-$d_{z^2-r^2} + d_{xz} + d_{yz}$, W-$d_{x^2+y^2} + d_{xy}$, and Te-$p_x + p_y$ orbitals [Figs. 4(d)–4(f)].

While strong coupling of the $p − d$ orbitals characterized the electronic states of the VLD systems, it also plays a significant role in determining the band splitting particularly near the Fermi level [Figs. 3(a)–3(c); Figs. 4(a)–4(c)]. It is generally understood that the coupling between atomic orbitals contributes to the nonzero SOC matrix element through the relation $\xi_l \langle \vec{L} \cdot \vec{S} \rangle_{u,v}$, where ξ_l is angular momentum
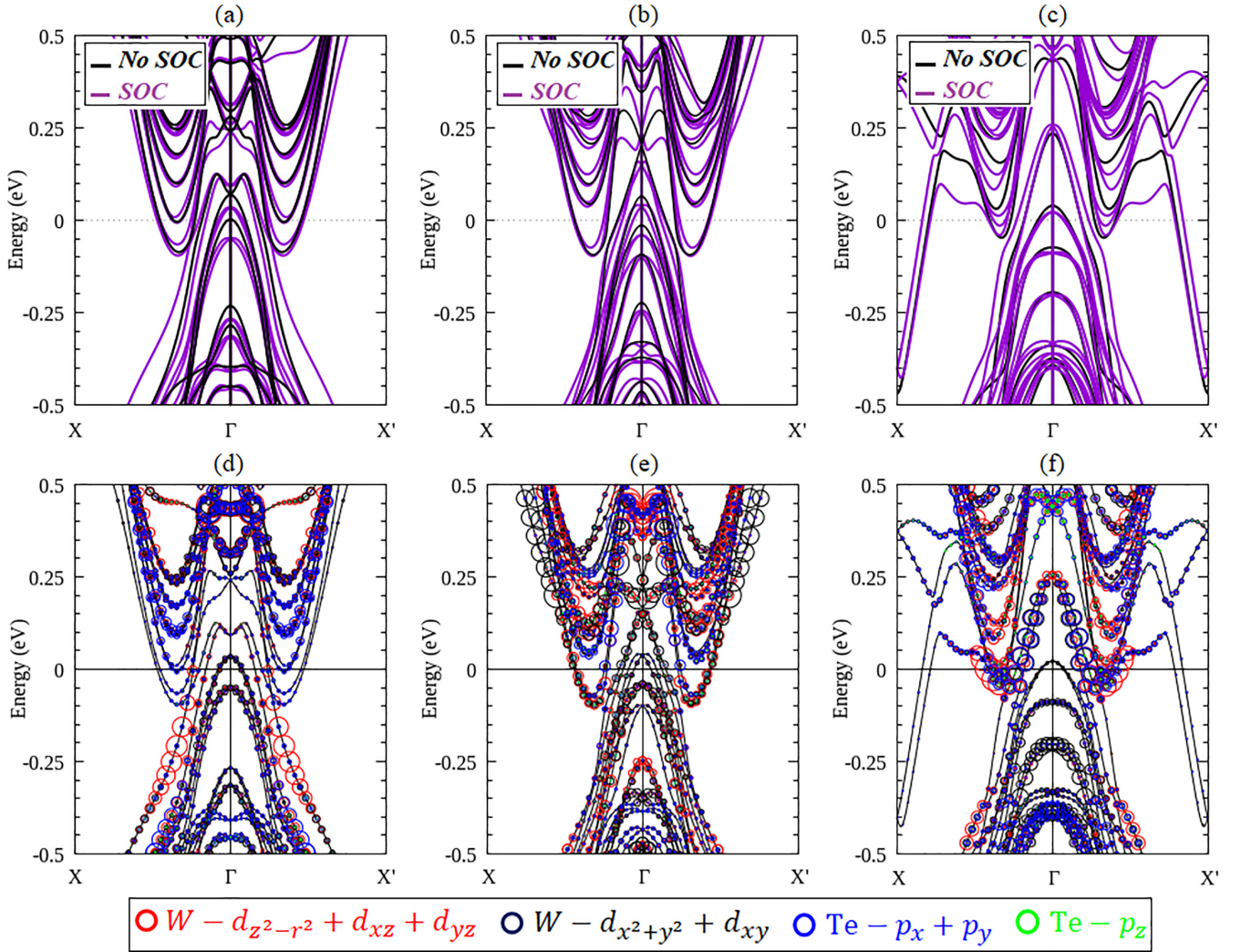
FIG. 4. Electronic structures of the zigzag-VLD systems. Electronic band structures calculated without (black lines) and with (red lines) the SOC for (a) ZZV_{Te_1}, (b) ZZV_{Te_2}, and (c) ZZV_W systems are shown. Orbital-resolved projected bands calculated for (d) ZZV_{Te_1}, (e) ZZV_{Te_2}, and (f) ZZV_W (g)–(i) systems are presented by the color circle, where the radii of the circles reflect the magnitude of the spectral weight of the particular orbitals to the bands.

resolved atomic SOC strength with $l = (s, p, d)$, $\vec{L}$ and $\vec{S}$ are the orbital angular momentum and Pauli spin operators, respectively, and (u, v) are the atomic orbitals. Consequently, only the orbitals with a nonzero magnetic quantum number ($m_l \neq 0$) will contribute to the spin splitting. For example, in the case of the ACV_{Te_1} system, the hybridization between $d_{x^2+y^2} + d_{xy}$ ($m_l \pm 2$) orbitals of W atoms and $p_x + p_y$ ($m_l \pm 1$) orbitals of the Te atoms around the VLD sites induces large spin splitting in the HOS bands at the $\vec{k}$ point along the $\Gamma - Y$ line [Fig. 3(e)]. Similar hybridization patterns inducing large spin splitting are also observed in other armchair-VLD systems (ACV_{Te_2} and ACV_W) at the LUS bands near the Y point [Figs. 3(d) and 3(f)] and the zigzag-VLD systems (ZZV_{Te_1}, ZZV_{Te_2}, and ZZV_W) at the LUS around the Γ point [Figs. 4(d)–4(f)]. These results are consistent with the established understanding that strong coupling of the in-plane $p - d$ orbitals plays a pivotal role in inducing significant spin splitting in defect states, as previously reported in various TMDCs ML [55,59–62].

To further analyze the spin-splitting properties of the VLD systems, we then focus on the two most stable VLD systems (ACV_{Te_1} and ACV_W) since they have the lowest formation energy E_f. We identify the largest spin-splitting energy in the bands at the HOS (ΔE_{HOS}) and LUS (ΔE_{LUS}) near the Fermi level as highlighted in Figs. 5(a) and 5(b), respectively. In the case of the ACV_{Te_1} system, we find that the calculated ΔE_{HOS} is 0.14 eV attained in the HOS, whereas ΔE_{LUS} diminishes to 0.04 eV in the LUS [Fig. 5(a)]. Conversely, when considering the ACV_W system, the HOS displays maximum spin-splitting energy ΔE_{HOS} of 0.037 eV, whereas the LUS exhibits higher spin-splitting energy ($\Delta E_{LUS} = 0.07$ eV) [Fig. 5(b)]. The stronger coupling between the W-$d_{x^2+y^2} + d_{xy}$ and Te-$p_x + p_y$ orbitals in the HOS of the ACV_{Te_1} system [Fig. 3(a)] is responsible for inducing the larger ΔE_{HOS}, while the mixing of the W-$d_{z^2-r^2} + d_{xz} + d_{yz}$ and Te-p_z orbitals in the HOS of the ACV_W system [Fig. 3(c)] contributes minimally to the ΔE_{HOS}. The same mechanism also explains the magnitude of the ΔE_{LUS} in both the ACV_{Te_1} and ACV_W systems.
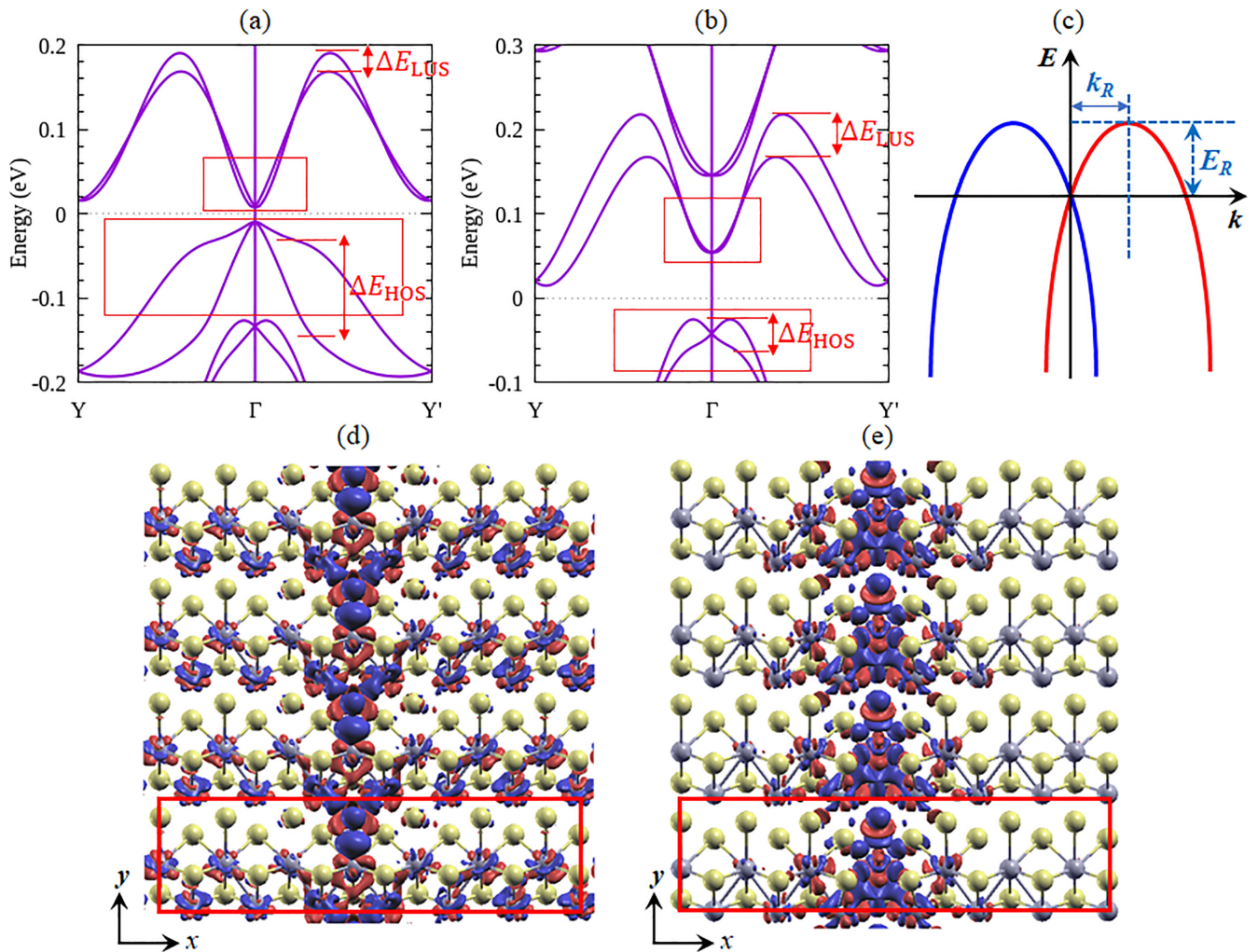
FIG. 5. Spin-split bands of the defect states along the $Y - \Gamma - Y$ line around the Fermi level calculated for the VLD systems: (a) ACV_{Te_1} and (b) ACV_W are presented. Here, the maximum spin splitting of ΔE_{HOS} and ΔE_{LUS} are highlighted in the HOS and LUS, respectively. (c) The schematic Rashba spin splitting near the degenerate states around the Γ point characterized by the Rashba energy E_R and the momentum offset k_R. The isosurface map of the different charge density calculated for (d) ACV_{Te_1} and (e) ACV_W is shown, where 0.005 was used as isovalue of the different electron density. The charge density is delocalized along the extended line defect (along the y direction), forming a quasi-1D conducting channel.

In addition, we also identified the obvious Rashba splitting around the Γ point in both the HOS and LUS [Figs. 5(a) and 5(b)]. We then quantify the strength of the Rashba splitting by calculating the Rashba parameter (α_R) through the relation, $\alpha_R = 2E_R/k_R$, where E_R and k_R are the parameters representing the Rashba energy and momentum offset defined schematically in Fig. 5(c). Here, E_R and k_R parameters are important to stabilize spin precession and achieve a phase offset for different spin channels in the S-FET device. It is revealed that the calculated Rashba parameters in both the HOS and LUS bands are $\alpha_R^{HOS} = 3.47$ eV Å, $\alpha_R^{LUS} = 0.21$ eV Å for the ACV_{Te_1} system and $\alpha_R^{HOS} = 1.49$ eV Å, $\alpha_R^{LUS} = 0.07$ eV Å for the ACV_W system. We summarize all the calculated results of the spin-splitting parameters including the ΔE_{HOS}, ΔE_{LUS}, α_R^{HOS}, and α_R^{LUS} in both the ACV_{Te_1} and ACV_W systems in Table II and compare these results with a few selected defective TMDCs ML systems from previously reported calculations. In particular, the calculated values of ΔE_{HOS} and α_R^{HOS} at the HOS of the ACV_{Te_1} system are the

largest among the defective systems observed on the 1H and 1T TMDCs MLs [55,59–62,66]. Remarkably, the associated SOC parameters discovered in the HOS and LUS of the VLDs are ample to enable the functionality of spintronics at room temperature.

It is important to note here that the spin-split bands with large spin-splitting energy are achieved in the HOS and LUS near the Fermi level, which is strongly dispersive along the $\Gamma - Y$ direction. This dispersive nature of the spin-split bands is strongly different from that observed in the SVD systems. Generally, most of the SVD systems exhibit dispersionless midgap defect states which occur due to the localized charge density around the vacancy site [61,65]. In contrast to our VLD systems, the strong interaction between neighboring W and Te atoms near the VLD site along the extended vacancy line leads to the dispersive spin-split bands at the HOS and LUS along the $\Gamma - Y$ direction [Figs. 5(a) and 5(b)]. The strong dispersive nature of the spin-split bands at the HOS and LUS can be further clarified by the calculated results of

TABLE II. Spin-splitting parameters including ΔE_{HOS} (eV), ΔE_{HOS} (eV), α_R^{HOS} (eV Å), and α_R^{LUS} (eV Å) calculated for the ACV_{Te_1} and ACV_W systems compared with those observed on a few selected defective TMDCs ML systems.

Systems	ΔE_{HOS} (eV)	ΔE_{LUS} (eV)	α_R^{HOS} (eV Å)	α_R^{LUS} (eV Å)	Reference
VLD in $1T'$-WTe$_2$ ML					
ACV_{Te_1}	0.14	0.04	3.47	0.21	This work
ACV_W	0.037	0.07	1.49	0.07	This work
VLD in $1T/1H$ TMDCs ML					
Se-VLD $1T$-PtSe$_2$			1.14	0.2	Ref. [55]
Double VLD $1H$-WSe$_2$				0.14–0.26	Ref. [59]
Chain doped WX_2				0.0–0.74	Ref. [66]
Chain doped MoX_2				0.1–1.0	Ref. [66]
SVD in $1T/1H$ TMDCs ML					
Se-SVD $1T$-PtSe$_2$	0.005	0.15			Ref. [60]
Se-SVD $1H$-WS$_2$		0.19			Ref. [61]
Halogen-doped $1T$-PtSe$_2$				0.01–1.7	Ref. [62]

the different charge densities presented in Figs. 5(d) and 5(e) for the ACV_{Te_1} and ACV_W systems, respectively. We find that both the VLD systems have delocalized charge density along the extended defect line, forming a quasi-1D conducting channel. This indicates that the 1D confined defect states emerge, implying that bandlike charge transport and higher mobility of the spin-split defect states are expected to be achieved [66,67], which is useful in transport-based electronic and spintronic devices.

To further characterize the nature of the spin-split defect states in both the LUS and HOS, we show in Figs. 6(a)–6(c) and 6(d)–6(f) the spin-resolved projected bands for the ACV_{Te_1} and ACV_W systems, respectively. It is revealed that both the VLDs exhibit the spin polarizations which are mostly characterized by S_x component of spin polarization along the entire path of the $\Gamma - Y$ line, while the other components (S_y, S_z) are almost zero. The existence of the in-plane mirror symmetry M_{yz} in both the ACV_{Te_1} and ACV_W systems enforces the spin components to hold the relation
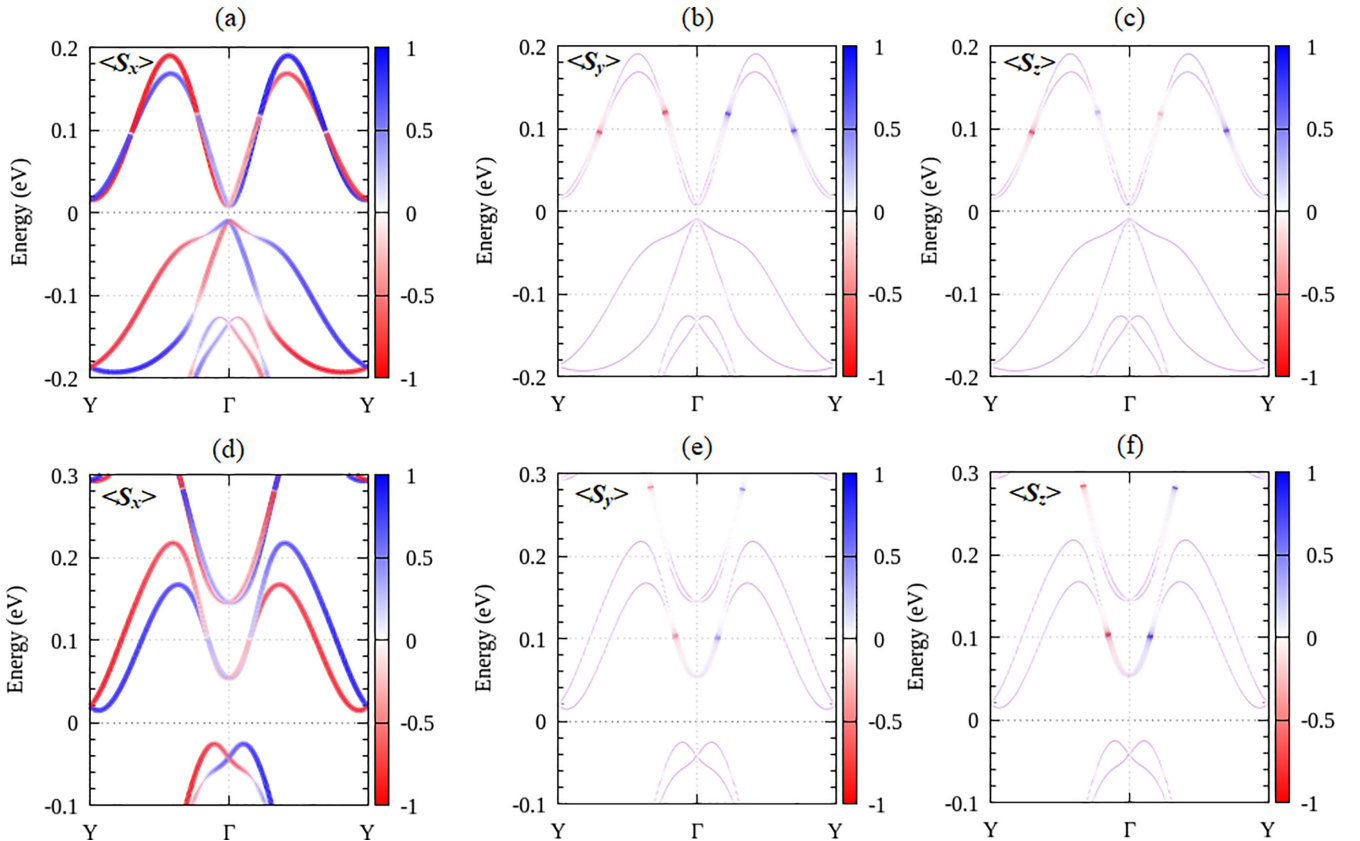
FIG. 6. Spin-resolved projected bands calculated for ACV_{Te_1} (a)–(c) and ACV_W (d)–(f) are shown. $\langle S_x \rangle$, $\langle S_y \rangle$, and $\langle S_z \rangle$ represent the expected values of the spin components as indicated by the color bar.

$(S_x, S_y, S_z) \rightarrow (S_x, -S_y, -S_z)$, which satisfies that only the in-plane S_x component is preserved. This indicates that a perfectly collinear spin configuration in the k space is achieved, which is oriented uniformly along the x direction. The appearance of the collinear spin configuration enforced by the in-plane mirror symmetry results in persistent spin textures as recently observed on bulk lead-free nonmagnetic materials [68], bulk WSi$_2$N$_4$ family [69], and various 2D materials [70–73]. This peculiar pattern of the spin configuration gives rise to the spatially periodic mode of the spin polarization, which protects the spin from decoherence and induces an extremely long spin lifetime [43–47].

To clarify the origin of the unidirectional spin polarization observed in the ACV_{Te_1} and ACV_{W} systems, we then apply $\vec{k} \cdot \vec{p}$ perturbation theory based on the group theory analysis. This approach enables us to derive an effective Hamiltonian for the spin-split states [74], as we applied recently to various defective systems in the 2D materials [55,60,62,75]. As previously mentioned, the pristine $1T'$-WTe$_2$ ML is centrosymmetric belonging to the C_{2h} point group. However, with the introduction of the VLDs, the structural symmetry is reduced. Due to time reversibility in the VLD systems, Kramer's degeneracy is conserved at the high symmetry k points in the FBZ such as Γ and Y points. Nevertheless, away from these time-reversal-invariant points, Kramer's doublet is perturbed due to the presence of SOC, which can be described through a $\vec{k} \cdot \vec{p}$ Hamiltonian. To further derive the effective SOC Hamiltonian, our initial focus centers on the vicinity of the Γ point, before extending our analysis to encompass all paths along the $\Gamma - Y$ line, where the symmetry group aligns with that of the Γ point.

Using the method introduced by Vajna *et al.*, the SOC Hamiltonian, denoted as $\hat{H}_{\text{SOC}}$, can be obtained through the following invariant expression [74]:

$$H_{\text{SOC}}(\vec{k}) = \alpha(g\vec{k}) \cdot [\det(g)g\vec{\sigma}], \quad (5)$$

where $\vec{k}$ and $\vec{\sigma}$ are the electron's wave vector and spin vector, respectively, and $\alpha(g\vec{k}) = \det(g)g\alpha(\vec{k})$, where g is the element of the point group characterizing the small group wave vector $G_{\vec{Q}}$ of the high symmetry point $\vec{Q}$ in the first Brillouin zone. By sorting out the components of $\vec{k}$ and $\vec{\sigma}$ according to irreducible representation (IR) of $G_{\vec{Q}}$, we can decompose again their direct product into IR. Notably, based on Eq. (5), only the IR components that are totally symmetric in this decomposition contribute to $\hat{H}_{\text{SOC}}$. Consequently, with the help of the corresponding tables of the point group, one can easily construct the possible term of $\hat{H}_{\text{SOC}}$.

In our VLD systems (ACV_{Te_1}, ACV_{W}), the structural symmetry is reduced to the C_s point group consisting of two elements: identity operation $E : (x, y, z) \rightarrow (x, y, z)$ and mirror symmetry operation $M_{yz} : (x, y, z) \rightarrow (-x, y, z)$. By using the character table and direct product table of the C_s point group, the component of the wave vector $\vec{k}$ and spin vector $\vec{\sigma}$ can be classified into the IRs of the C_s point group. By applying the table of the direct product of the C_s point group, the possible combination of the $\vec{k}$ and $\vec{\sigma}$ components up to nth order in $\vec{k}$ can be obtained; thus the effective SOC Hamiltonian $\hat{H}_{\text{SOC}}$ up to nth order in $\vec{k}$ near the Γ point can be written

TABLE III. Rashba parameters [α_1 (eV Å), α_3 (eV Å^3)] of the VLD systems (ACV_{Te_1}, ACV_{W}) obtained by fitting DFT bands of the VLDs at the HOS and LUS up to the third order term $\vec{k}$ of Eq. (7). The carrier effective mass, m^*, is also obtained from the fitting of the DFT bands, which is calculated in the unit of m_0, where m_0 is the electron rest mass. The wavelength of the spin-polarized states, denoted as L_{SP} (in nm), are also estimated by the relations $L_{\text{SP}} = (\pi \hbar^2)/(m^* \alpha_1)$.

Spin-split states	m^* (m_0)	α_1 (eV Å)	α_3 (eV Å^3)	L_{SP} (nm)
ACV_{Te_1} system				
HOS	−1.1	3.64	−64.94	4.42
LUS	1.3	0.25	−122.08	159.5
ACV_{W} system				
HOS	−1.25	1.56	−17.31	8.47
LUS	1.3	0.09	−37.07	197.9

as (see Supplemental Material [76] for the detail derivation which includes Ref. [74] therein)

$$\begin{aligned} H_{\text{SOC}}(\vec{k}) = {} & \alpha_1 k_y \sigma_x + \beta_1 k_x \sigma_y + \gamma_1 k_x \sigma_z + \delta_1 k_z \sigma_x \\ & + \alpha_3 k_y^3 \sigma_x + \beta_3 k_x^3 \sigma_y + \gamma_3 k_x^3 \sigma_z + \delta_3 k_z^3 \sigma_z \\ & + \cdots + \alpha_n k_y^n \sigma_x + \beta_n k_x^n \sigma_y + \gamma_n k_x^n \sigma_z + \delta_n k_z^n \sigma_x, \end{aligned}$$
$$(6)$$

where α_n, β_n, γ_n, and δ_n are the nth order in $\vec{k}$ SOC parameters. However, due to the 1D nature of the spin-split states along the extended defect line (y direction), all the terms containing k_x and k_z components should vanish. Therefore, Eq. (6) can be rewritten as

$$H_{\text{SOC}}(\vec{k}) = \alpha_1 k_y \sigma_x + \alpha_3 k_y^3 \sigma_x + \alpha_5 k_y^5 \sigma_x + \cdots + \alpha_n k_y^n \sigma_x. \quad (7)$$

Equation (7) reveals that $\hat{H}_{\text{SOC}}$ is primarily defined by the σ_x term, indicating a uniform spin polarization aligned along the x axis near the Γ point. This observation is consistent with the findings in our spin-resolved projected bands depicted in Fig. 6, which were obtained through DFT calculations. Furthermore, when we move away from the Γ point to the $\vec{k}$ point along the $\Gamma - Y$ direction, higher-order $\vec{k}$ terms come into play. Nevertheless, as demonstrated in Eq. (7), the σ_x component of the spin vector remains conserved even at higher-order $\vec{k}$ terms, preserving the unidirectional spin polarization at larger wave vectors $\vec{k}$ within the FBZ.

For quantitative analysis, we performed fitting calculations of our model in Eq. (7) to the DFT bands in both the HOS and LUS, aiming to determine the Rashba coefficients up to third-order $\vec{k}$ terms (α_1, α_3); see Fig. S1 in the Supplemental Material [76] for the detailed calculations. The computed parameters are presented in Table III. For the ACV_{Te1} system, we found that $\alpha_1 = 3.64$ eV Å, $\alpha_3 = -64.94$ eV Å^3 for the HOS and $\alpha_1 = 0.25$ eV Å, $\alpha_3 = -122.08$ eV Å^3 for the LUS. Conversely, for the ACV_{W} system, the values were $\alpha_1 = 1.56$ eV Å, $\alpha_3 = -17.31$ eV Å^3 for the HOS and $\alpha_1 = 0.09$ eV Å, $\alpha_3 = -37.07$ eV Å^3 for the LUS. Notably, the calculated α_3 parameters for the spin-split bands at the HOS and LUS in both the VLD systems are sufficiently large, indicating the significance of the third-order term in Eq. (7) for determining the spin-splitting characteristics of the bands. However, the computed
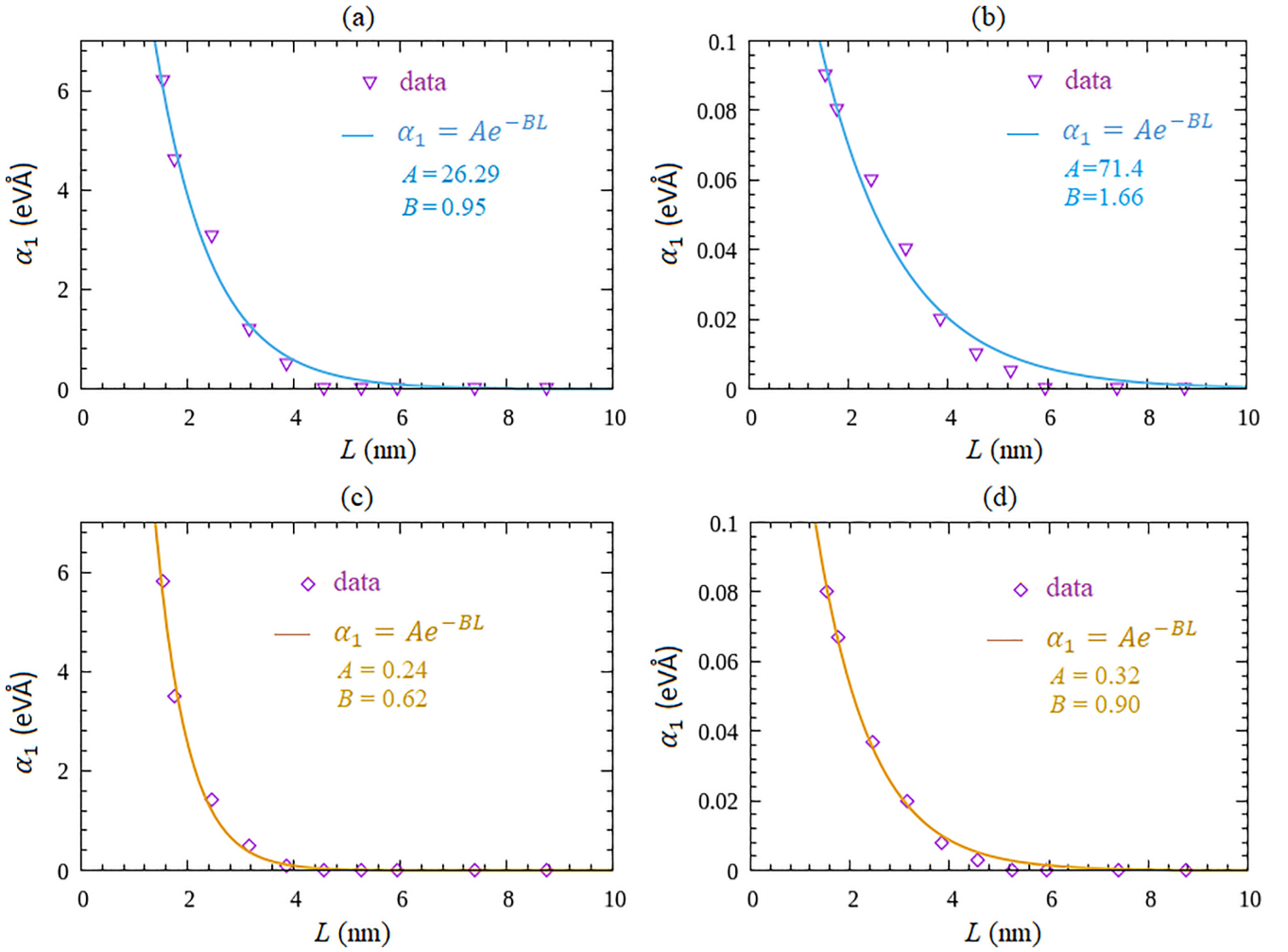
FIG. 7. Variation of the α_1 with the supercell length calculated at (a) HOS and (b) LUS of the ACV_{Te_1} system is shown. (c),(d) Same with (a),(b) but for the ACV_W system. A parametrization of α_1 as a function of the supercell size L along the armchair direction is performed by using the relation $\alpha_1(L) = A \exp^{-BL}$, where A and B are the parameters obtained by fitting calculation.

first-order parameters α_1 are closely aligned with the values obtained using the relation $\alpha = 2E_R/k_R$ as shown in Table II, thereby confirming the consistency of our fitting calculations.

Additionally, utilizing the calculated values of α_1, we can estimate the spatial wavelength of the spin-polarized states using the relation $L_{SP} = (\pi \hbar^2)/(m^* \alpha_1)$ [45], where m^* is the effective carrier mass. Here, m^* is calculated by fitting the band dispersion around the HOS and LUS. Table III shows the calculated L_{SP} at the HOS and LUS for the ACV_{Te_1} and ACV_W systems. It is revealed that the calculated L_{SP} at the HOS of the ACV_{Te_1} system is 4.42 nm, which is much smaller than that of the ACV_W system ($L_{SP} = 8.46$ nm). This value also ranks as the smallest among the VLDs systems observed on the $1H$-WSe$_2$ ML ($L_{SP} = 8.56$–10.18 nm) [59] and $1T$-PtSe$_2$ ML ($L_{SP} = 6.33$–29.47 nm) [55]. Importantly, this value of L_{SP} is three orders of magnitude smaller than that observed in semiconductor heterostructures ($L_{SP} = 5$–10 μm) [77,78], signifying the promise of the current system for miniaturization spintronics devices.

Next, we discussed the properties of the Rashba splitting observed in the VLD-engineered $1T'$-WTe$_2$ ML by considering the effect of the supercell size. We noted here

that the observed Rashba splitting in the HOS and LUS of the VLD systems reflects the 1D spin-split confined defect states along the extended line defect [Figs. 5(a) and 5(b); Figs. 5(d) and 5(e)]. Consistent with the widely observed confined defect states reported on various 2D TMDCs [55,59,66], the appearance of the 1D spin-split confined defect states in the current system, which are mostly characterized by the $p - d$ coupling orbitals [Figs. 3(d) and 3(f)], are accumulated significantly on the VLD site and penetrated rapidly into the bulk with the exponential decay as confirmed by the charge spreading in the different charge densities shown in Figs. 5(d) and 5(e). Accordingly, for the VLD systems with smaller supercell sizes, the interaction between the periodic defect images strengthens the coupling of the in-plane $p - d$ orbitals in the spin-split defect states and hence increases the Rashba splitting. On the contrary, increasing the supercell size of the VLD systems decreases the periodic defect image interactions, resulting in the spin-split defect states becoming more localized with much smaller Rashba splitting. The rapid decreases of the Rashba splitting under the increase of the supercell sizes are further well described through the exponential dependent model. In Figs. 7(a) and 7(b),

we present the exponential fitting of the linear Rashba SOC parameter α_1 as a function of the supercell size (L) calculated at the HOS and LUS for the ACV_{Te_1} system, respectively, while those calculated for the ACV_W system are shown in Figs. 7(c) and 7(d), respectively. Here, a parametrization of α_1 as a function of L was performed by the following exponential function, $\alpha_1(L) = A \exp^{-BL}$, where A and B are the parameters obtained by fitting calculation; see the inset of Figs. 7(a)–7(d). As expected, we find that the calculated α_1 at both the HOS and LUS tends to reduce as the thickness of the supercell of the VLD systems increases. Therefore, the Rashba splitting at the HOS and LUS can be adjusted by choosing an adequate thickness of the VLDs supercell.

Now, we discuss the possibility of realizing the VLD-engineered $1T'$-WTe$_2$ ML in the spintronics device applications. Here, we envision that it is possible to apply our VLD systems as an ideal 1D-Rashba channel in the SFET devices [79]. Considering the fact that the presence of the VLD systems exhibits perfectly collinear spin polarization, the spin-polarized currents can be effectively generated without any dissipation, thus increasing the performance of the SFET devices. This can be achieved by employing the lithographic patterning technique [80,81], which is compatible with current technology, to create arrays of line defects. In fact, fabrication of the 1D edge step of $1T'$-WTe2 has been recently reported experimentally [41,42], suggesting that the realization of our VLDs' systems for the device's application is now a feasible prospect.

Before concluding, we would like to discuss the potential physical implications of the observed 1D confined defect states in both the ACV_{Te_1} and ACV_W systems, correlated to their topological characteristics. Previously, the pristine $1T'$-WTe2 ML has been reported as a quantum spin Hall insulator (QSHI) [27], featuring a quantized Hall conductance in the absence of a magnetic field originated from topologically protected 1D degenerated metallic edge states and an insulating bulk gap driven by band inversion and the strong SOC. Different from the spin-degenerate parabolic dispersion of the conventional 1D metallic systems, the QSHI host linearly dispersing 1D edge states displaying a degenerate helical-fermion mode where the spin polarity is locked to the crystal momentum (helicity) [82]. In addition, the presence of the 1D helical-fermion edge states also induces the so-called Tomonaga-Luttinger liquid (TLL) behavior [83], in which the strong SOC causes the spin and chirality indices to coincide, resulting in mixed bosonic excitations involving these two degrees of freedom. In contrast to the pristine system, both the ACV_{Te_1} and ACV_W systems exhibit 1D spin-split polarized confined defect states where the band gap is consistently present [Figs. 4(a)–4(c)], indicating that the QSHI state does not exist. The absence of the QHSI in the spin-split confined defect states can be further confirmed by inspecting the topological nature of the electronic bands in the 2D defective bulk structure of the ACV_{Te_1} and ACV_W systems composed of a sequence of single square cells with point defect as shown in Fig. S2 in the Supplemental Material [76]. Here, we calculate the Z_2 topological invariant at the parity of the occupied bands at the time-reversal invariant points; see the Supplemental Material [76] for the detailed methods, which includes Refs. [84–87] therein. Compared with the pristine system ($Z_2 = 1$), our

calculation revealed that $Z_2 = 0$ for the 2D defective bulk structures, confirming that these systems are indeed trivial insulators. Even though our VLD systems did not feature the QSHI, the occurrence of the large spin-splitting bands with perfectly unidirectional spin configuration in the 1D confined defect states (Fig. 6) provides more advantages for spintronics application due to the protection of the spin from decoherence and the extremely long spin lifetime [43–47].

IV. CONCLUSION

The effect of the line defect on the electronic properties of the $1T'$ WTe$_2$ ML has been systematically investigated by employing the first-principles DFT calculations supplemented by $\vec{k} \cdot \vec{p}$ based-symmetry analysis. We have considered six different configurations of the VLD extended. The armchair-VLDs include a Te$_1$ armchair-VLD (ACV_{Te_1}), Te$_2$ armchair-VLD (ACV_{Te_2}), and W armchair-VLD (ACV_W), while the zigzag-VLDs comprise a Te$_1$ zigzag-VLD (ZZV_{Te_1}), Te$_2$ zigzag-VLD (ZZV_{Te_2}), and W zigzag-VLD (ZZV_W), where Te$_1$ and Te$_2$ are two nonequivalent Te atoms located at the lower and higher sites in the top layer, respectively. We revealed that both the ACV_{Te_1} and ACV_W systems have the lowest formation energy E_f. By evaluating the two stablest VLD systems (ACV_{Te_1}, ACV_W), we have observed large spin-splitting energy in the bands near the Fermi level, which is mainly originated from the strong $p - d$ coupling of the electronic states. Importantly, we observed strong Rashba states with perfectly collinear spin configurations in the momentum space. This special spin configuration may induce a specific spin mode that protects the spin from decoherence and leads to an extremely long spin lifetime [43–47]. Furthermore, we have confirmed that the observed unidirectional Rashba states are enforced by the inversion symmetry breaking and the 1D nature of the VLD, as clarified by the $\vec{k} \cdot \vec{p}$ model derived from the symmetry analysis. Our discoveries open up a potential avenue for inducing significant spin splitting in the $1T'$-WTe$_2$ ML, a development that holds great significance in the creation of exceptionally effective spintronic devices.

The findings presented in this article offer insights into the spin-orbit coupling (SOC) behavior within the $1T'$-WTe$_2$ ML, which contains the most commonly observed VLDs. These outcomes are likely applicable to other ML systems with similar structures and electronic characteristics, such as MoTe$_2$ ML [88,89]. Specifically, the potential to control these SOC-induced spin-split states is a subject worthy of further investigation, given their high promise in spintronics applications. It would be intriguing to explore the possibility of spin reversal under the influence of an applied electric field. However, delving deeper into this topic goes beyond the scope of this paper and will be the focus of future research.

ACKNOWLEDGMENTS

[1] X. Cui, G.-H. Lee, Y. D. Kim, G. Arefe, P. Y. Huang, C.-H. Lee, D. A. Chenet, X. Zhang, L. Wang, F. Ye, F. Pizzocchero, B. S. Jessen, K. Watanabe, T. Taniguchi, D. A. Muller, T. Low, P. Kim, and J. Hone, Multi-terminal transport measurements of MoS$_2$ using a van der Waals heterostructure device platform, Nat. Nanotechnol. **10**, 534 (2015).

[2] R. Cheng, D. Li, H. Zhou, C. Wang, A. Yin, S. Jiang, Y. Liu, Y. Chen, Y. Huang, and X. Duan, Electroluminescence and photocurrent generation from atomically sharp WSe$_2$/MoS$_2$ heterojunction *p–n* diodes, Nano Lett. **14**, 5590 (2014).

[3] Q. H. Wang, K. Kalantar-Zadeh, A. Kis, J. N. Coleman, and M. S. Strano, Electronics and optoelectronics of two-dimensional transition metal dichalcogenides, Nat. Nanotechnol. **7**, 699 (2012).

[4] A. Avsar, H. Ochoa, F. Guinea, B. Özyilmaz, B. J. van Wees, and I. J. Vera-Marun, Colloquium: Spintronics in graphene and other two-dimensional materials, Rev. Mod. Phys. **92**, 021003 (2020).

[5] A. Kononov, G. Abulizi, K. Qu, J. Yan, D. Mandrus, K. Watanabe, T. Taniguchi, and C. Schönenberger, One-dimensional edge transport in few-layer WTe$_2$, Nano Lett. **20**, 4228 (2020).

[6] D. MacNeill, G. M. Stiehl, M. H. D. Guimaraes, R. A. Buhrman, J. Park, and D. C. Ralph, Control of spin–orbit torques through crystal symmetry in WTe$_2$/ferromagnet bilayers, Nat. Phys. **13**, 300 (2017).

[7] S. Manzeli, D. Ovchinnikov, D. Pasquier, O. V. Yazyev, and A. Kis, 2d transition metal dichalcogenides, Nat. Rev. Mater. **2**, 17033 (2017).

[8] K. S. Novoselov, D. Jiang, F. Schedin, T. J. Booth, V. V. Khotkevich, S. V. Morozov, and A. K. Geim, Two-dimensional atomic crystals, Proc. Natl. Acad. Sci. USA **102**, 10451 (2005).

[9] D. Voiry, A. Mohite, and M. Chhowalla, Phase engineering of transition metal dichalcogenides, Chem. Soc. Rev. **44**, 2702 (2015).

[10] U. Patil and N. M. Caffrey, Composition dependence of the charge-driven phase transition in group-VI transition metal dichalcogenides, Phys. Rev. B **100**, 075424 (2019).

[11] X. Qian, J. Liu, L. Fu, and J. Li, Quantum spin Hall effect in two-dimensional transition metal dichalcogenides, Science **346**, 1344 (2014).

[12] Y. Tao, J. A. Schneeloch, A. A. Aczel, and D. Louca, T_d to $1T'$ structural phase transition in the WTe$_2$ weyl semimetal, Phys. Rev. B **102**, 060103(R) (2020).

[13] M. P. Singh, J. Kiemle, I. Ozdemir, P. Zimmermann, T. Taniguchi, K. Watanabe, M. Burghard, O. U. Akturk, C. Kastl, and A. W. Holleitner, Impact of domain disorder on optoelectronic properties of layered semimetal MoTe$_2$, 2D Mater. **9**, 011002 (2022).

[14] C. Zhao, M. Hu, J. Qin, B. Xia, C. Liu, S. Wang, D. D. Guan, Y. Li, H. Zheng, J. Liu, and J. Jia, Strain tunable semimetal–topological-insulator transition in monolayer $1T'$-WTe$_2$, Phys. Rev. Lett. **125**, 046801 (2020).

[15] S.-Y. Xu, Q. Ma, H. Shen, V. Fatemi, S. Wu, T.-R. Chang, G. Chang, A. M. M. Valdivia, C.-K. Chan, Q. D. Gibson, J. Zhou, Z. Liu, K. Watanabe, T. Taniguchi, H. Lin, R. J. Cava, L. Fu, N. Gedik, and P. Jarillo-Herrero, Electrically switchable berry curvature dipole in the monolayer topological insulator WTe$_2$, Nat. Phys. **14**, 900 (2018).

[16] Z. Y. Zhu, Y. C. Cheng, and U. Schwingenschlögl, Giant spin-orbit-induced spin splitting in two-dimensional transition-metal dichalcogenide semiconductors, Phys. Rev. B **84**, 153402 (2011).

[17] K. Kośmider, J. W. González, and J. Fernández-Rossier, Large spin splitting in the conduction band of transition metal dichalcogenide monolayers, Phys. Rev. B **88**, 245436 (2013).

[18] M. A. U. Absor, H. Kotaka, F. Ishii, and M. Saito, Strain-controlled spin splitting in the conduction band of monolayer WS$_2$, Phys. Rev. B **94**, 115131 (2016).

[19] Y. Affandi and M. A. Ulil Absor, Electric field-induced anisotropic rashba splitting in two dimensional tungsten dichalcogenides WX$_2$ (*X*: S, Se, Te): A first-principles study, Physica E **114**, 113611 (2019).

[20] S. Guo, Y. Wang, C. Wang, Z. Tang, and J. Zhang, Large spin-orbit splitting in the conduction band of halogen (F, Cl, Br, and I) doped monolayer Ws$_2$ with spin-orbit coupling, Phys. Rev. B **96**, 245305 (2017).

[21] H. Bragança, R. Vasconcelos, J. Fu, R. P. D'Azevedo, D. R. da Costa, A. L. A. Fonseca, and F. Qu, Magnetic brightening, large valley Zeeman splitting, and dynamics of long-lived A and B dark excitonic states in monolayer WS$_2$, Phys. Rev. B **100**, 115306 (2019).

[22] M. A. Cazalilla, H. Ochoa, and F. Guinea, Quantum spin Hall effect in two-dimensional crystals of transition-metal dichalcogenides, Phys. Rev. Lett. **113**, 077201 (2014).

[23] R.-L. Chu, X. Li, S. Wu, Q. Niu, W. Yao, X. Xu, and C. Zhang, Valley-splitting and valley-dependent inter-Landau-level optical transitions in monolayer MoS$_2$ quantum Hall systems, Phys. Rev. B **90**, 045427 (2014).

[24] Z. Gong, G.-B. Liu, H. Yu, D. Xiao, X. Cui, X. Xu, and W. Yao, Magnetoelectric effects and valley-controlled spin quantum gates in transition metal dichalcogenide bilayers, Nat. Commun. **4**, 2053 (2013).

[25] B. Radisavljevic, A. Radenovic, J. Brivio, V. Giacometti, and A. Kis, Single-layer MoS$_2$ transistors, Nat. Nanotechnol. **6**, 147 (2011).

[26] F. Zheng, C. Cai, S. Ge, X. Zhang, X. Liu, H. Lu, Y. Zhang, J. Qiu, T. Taniguchi, K. Watanabe, S. Jia, J. Qi, J.-H. Chen, D. Sun, and J. Feng, On the quantum spin Hall gap of monolayer $1T'$- WTe$_2$, Adv. Mater. **28**, 4845 (2016).

[27] S. Tang, C. Zhang, D. Wong, Z. Pedramrazi, H.-Z. Tsai, C. Jia, B. Moritz, M. Claassen, H. Ryu, S. Kahn, J. Jiang, H. Yan, M. Hashimoto, D. Lu, R. G. Moore, C.-C. Hwang, C. Hwang, Z. Hussain, Y. Chen, M. M. Ugeda *et al.*, Quantum spin Hall state in monolayer $1T'$-WTe$_2$, Nat. Phys. **13**, 683 (2017).

[28] C. H. Naylor, W. M. Parkin, Z. Gao, H. Kang, M. Noyan, R. B. Wexler, L. Z. Tan, Y. Kim, C. E. Kehayias, F. Streller, Y. R. Zhou, R. Carpick, Z. Luo, Y. W. Park, A. M. Rappe, M. Drndić, J. M. Kikkawa, and A. T. C. Johnson, Large-area synthesis of high-quality monolayer $1T'$-WTe$_2$ flakes, 2D Mater. **4**, 021008 (2017).

[29] W. Zhao, E. Runburg, Z. Fei, J. Mutch, P. Malinowski, B. Sun, X. Huang, D. Pesin, Y.-T. Cui, X. Xu, J.-H. Chu, and D. H. Cobden, Determination of the spin axis in quantum spin Hall insulator candidate monolayer WTe$_2$, Phys. Rev. X **11**, 041034 (2021).

[30] C. Tan, M.-X. Deng, G. Zheng, F. Xiang, S. Albarakati, M. Algarni, L. Farrar, S. Alzahrani, J. Partridge, J. B. Yi, A. R. Hamilton, R.-Q. Wang, and L. Wang, Spin-momentum

locking induced anisotropic magnetoresistance in monolayer WTe$_2$, Nano Lett. **21**, 9005 (2021).

[31] Y.-M. Xie, B. T. Zhou, and K. T. Law, Spin-orbit-parity-coupled superconductivity in topological monolayer WTe$_2$, Phys. Rev. Lett. **125**, 107001 (2020).

[32] L.-K. Shi and J. C. W. Song, Symmetry, spin-texture, and tunable quantum geometry in a WTe$_2$ monolayer, Phys. Rev. B **99**, 035403 (2019).

[33] J. H. Garcia, J. You, M. García-Mota, P. Koval, P. Ordejón, R. Cuadrado, M. J. Verstraete, Z. Zanolli, and S. Roche, Electrical control of spin-polarized topological currents in monolayer WTe$_2$, Phys. Rev. B **106**, L161410 (2022).

[34] J. H. Garcia, M. Vila, C.-H. Hsu, X. Waintal, V. M. Pereira, and S. Roche, Canted persistent spin texture and quantum spin Hall effect in WTe$_2$, Phys. Rev. Lett. **125**, 256603 (2020).

[35] M. Vila, C.-H. Hsu, J. H. Garcia, L. A. Benítez, X. Waintal, S. O. Valenzuela, V. M. Pereira, and S. Roche, Low-symmetry topological materials for large charge-to-spin interconversion: The case of transition metal dichalcogenide monolayers, Phys. Rev. Res. **3**, 043230 (2021).

[36] P. Li, W. Wu, Y. Wen, C. Zhang, J. Zhang, S. Zhang, Z. Yu, S. A. Yang, A. Manchon, and X.-x. Zhang, Spin-momentum locking and spin-orbit torques in magnetic nano-heterojunctions composed of weyl semimetal WTe$_2$, Nat. Commun. **9**, 3990 (2018).

[37] I. Ozdemir, A. W. Holleitner, C. Kastl, and O. Ü. Aktürk, Thickness and defect dependent electronic, optical and thermoelectric features of WTe$_2$, Sci. Rep. **12**, 12756 (2022).

[38] L. Muechler, W. Hu, L. Lin, C. Yang, and R. Car, Influence of point defects on the electronic and topological properties of monolayer WTe$_2$, Phys. Rev. B **102**, 041103(R) (2020).

[39] H.-Y. Song and J.-T. Lü, Single-site point defects in semimetal WTe$_2$: A density functional theory study, AIP Adv. **8**, 125323 (2018).

[40] W.-H. Chen, N. Kawakami, J.-J. Lin, H.-I. Huang, R. Arafune, N. Takagi, and C.-L. Lin, Noncentrosymmetric characteristics of defects on WTe$_2$, Phys. Rev. B **106**, 075428 (2022).

[41] L. Peng, Y. Yuan, G. Li, X. Yang, J.-J. Xian, C.-J. Yi, Y.-G. Shi, and Y.-S. Fu, Observation of topological states residing at step edges of WTe$_2$, Nat. Commun. **8**, 659 (2017).

[42] A. Lau, R. Ray, D. Varjas, and A. R. Akhmerov, Influence of lattice termination on the edge states of the quantum spin Hall insulator monolayer 1T'-WTe$_2$, Phys. Rev. Mater. **3**, 054206 (2019).

[43] M. I. Dyakonov and V. I. Perel, Spin relaxation of conduction electrons in noncentrosymmetric semiconductors, Sov. Phys. Solid State **13**, 3023 (1972).

[44] J. Schliemann, J. C. Egues, and D. Loss, Nonballistic spin-field-effect transistor, Phys. Rev. Lett. **90**, 146801 (2003).

[45] B. A. Bernevig, J. Orenstein, and S.-C. Zhang, Exact SU(2) symmetry and persistent spin helix in a spin-orbit coupled system, Phys. Rev. Lett. **97**, 236601 (2006).

[46] J. Schliemann, Colloquium: Persistent spin textures in semiconductor nanostructures, Rev. Mod. Phys. **89**, 011001 (2017).

[47] P. Altmann, M. P. Walser, C. Reichl, W. Wegscheider, and G. Salis, Suppressed decay of a laterally confined persistent spin helix, Phys. Rev. B **90**, 201306(R) (2014).

[48] T. Ozaki, Variationally optimized atomic orbitals for large-scale electronic structures, Phys. Rev. B **67**, 155108 (2003).

[49] T. Ozaki and H. Kino, Numerical atomic basis orbitals from H to Kr, Phys. Rev. B **69**, 195113 (2004).

[50] T. Ozaki and H. Kino, Efficient projector expansion for the *ab initio* LCAO method, Phys. Rev. B **72**, 045121 (2005).

[51] J. P. Perdew, K. Burke, and M. Ernzerhof, Generalized gradient approximation made simple, Phys. Rev. Lett. **77**, 3865 (1996).

[52] W. Kohn and L. J. Sham, Self-consistent equations including exchange and correlation effects, Phys. Rev. **140**, A1133 (1965).

[53] K. Lejaeghere, G. Bihlmayer, T. Björkman, P. Blaha, S. Blügel, V. Blum, D. Caliste, I. E. Castelli, S. J. Clark, A. Dal Corso, S. de Gironcoli, T. Deutsch, J. K. Dewhurst, I. Di Marco, C. Draxl, M. Dułak, O. Eriksson, J. A. Flores-Livas, K. F. Garrity, L. Genovese *et al.*, Reproducibility in density functional theory calculations of solids, Science **351**, aad3000 (2016).

[54] C. Freysoldt, B. Grabowski, T. Hickel, J. Neugebauer, G. Kresse, A. Janotti, and C. G. Van de Walle, First-principles calculations for point defects in solids, Rev. Mod. Phys. **86**, 253 (2014).

[55] M. A. U. Absor, I. Santoso, N. Yamaguchi, and F. Ishii, Spin splitting with persistent spin textures induced by the line defect in the 1T phase of monolayer transition metal dichalcogenides, Phys. Rev. B **101**, 155410 (2020).

[56] H. Kotaka, F. Ishii, and M. Saito, Rashba effect on the structure of the Bi one-bilayer film: Fully relativistic first-principles calculation, Jpn. J. Appl. Phys. **52**, 035204 (2013).

[57] E. Torun, H. Sahin, S. Cahangirov, A. Rubio, and F. M. Peeters, Anisotropic electronic, mechanical, and optical properties of monolayer WTe$_2$, J. Appl. Phys. **119**, 074307 (2016).

[58] W. Yang, Z.-Y. Yuan, Y.-Q. Luo, Y. Yang, F.-W. Zheng, Z.-H. Hu, X.-H. Wang, Y.-A. Liu, and P. Zhang, Raman-active modes of 1T'-WTe$_2$ under tensile strain: A first-principles prediction, Phys. Rev. B **99**, 235401 (2019).

[59] X. Li, S. Zhang, H. Huang, L. Hu, F. Liu, and Q. Wang, Unidirectional spin–orbit interaction induced by the line defect in monolayer transition metal dichalcogenides for high-performance devices, Nano Lett. **19**, 6005 (2019).

[60] M. A. U. Absor, I. Santoso, Harsojo, K. Abraha, F. Ishii, and M. Saito, Defect-induced large spin-orbit splitting in monolayer PtSe$_2$, Phys. Rev. B **96**, 115128 (2017).

[61] W.-F. Li, C. Fang, and M. A. van Huis, Strong spin-orbit splitting and magnetism of point defect states in monolayer WS$_2$, Phys. Rev. B **94**, 195425 (2016).

[62] M. A. U. Absor, I. Santoso, Harsojo, K. Abraha, H. Kotaka, F. Ishii, and M. Saito, Strong rashba effect in the localized impurity states of halogen-doped monolayer PtSe$_2$, Phys. Rev. B **97**, 205138 (2018).

[63] H.-P. Komsa and A. V. Krasheninnikov, Native defects in bulk and monolayer MoS$_2$ from first principles, Phys. Rev. B **91**, 125304 (2015).

[64] J.-Y. Noh, H. Kim, and Y.-S. Kim, Stability and electronic structures of native defects in single-layer MoS$_2$, Phys. Rev. B **89**, 205417 (2014).

[65] W. Zhang, H. T. Guo, J. Jiang, Q. C. Tao, X. J. Song, H. Li, and J. Huang, Magnetism and magnetocrystalline anisotropy in single-layer PtSe2: Interplay between strain and vacancy, J. Appl. Phys. **120**, 013904 (2016).

[66] M. Gupta, A. Chauhan, S. Satpathy, and B. R. K. Nanda, Electron confinement in chain-doped transition metal dichalcogenides: A platform for spin-orbit coupled one-dimensional physics, Phys. Rev. B **108**, 075139 (2023).

[67] I. I. Fishchuk, A. Kadashchuk, A. Bhoolokam, A. de Jamblinne de Meux, G. Pourtois, M. M. Gavrilyuk, A. Köhler, H. Bässler, P. Heremans, and J. Genoe, Interplay between hopping and band transport in high-mobility disordered semiconductors at large carrier concentrations: The case of the amorphous oxide ingazno, Phys. Rev. B **93**, 195204 (2016).

[68] S. Sheoran, P. Bhumla, and S. Bhattacharya, Emergence of cubic ordered full-plane persistent spin textures in lead-free materials, Phys. Rev. Mater. **6**, 094602 (2022).

[69] S. Sheoran, S. Monga, A. Phutela, and S. Bhattacharya, Coupled spin-valley, Rashba effect, and hidden spin polarization in WSi$_2$N$_4$ family, J. Phys. Chem. Lett. **14**, 1494 (2023).

[70] S. A. Sasmito, M. Anshory, I. Jihad, and M. A. U. Absor, Reversible spin textures with giant spin splitting in two-dimensional GaXY (X = Se, Te; Y = Cl, Br, I) compounds for a persistent spin helix, Phys. Rev. B **104**, 115145 (2021).

[71] M. A. U. Absor and F. Ishii, Intrinsic persistent spin helix state in two-dimensional group-IV monochalcogenide MX monolayers (M = Sn or Ge and X = S, Se, or Te), Phys. Rev. B **100**, 115104 (2019).

[72] S.-D. Guo, X.-K. Feng, D. Huang, S. Chen, G. Wang, and Y. S. Ang, Intrinsic persistent spin texture in two-dimensional T-XY (X, Y = P, As, Sb, Bi; $X \neq Y$), Phys. Rev. B **108**, 075421 (2023).

[73] M. K. Mohanta and P. Jena, Symmetry-driven persistent spin texture for the two-dimensional nonsymmorphic CdTe and ZnTe crystal structures, Phys. Rev. B **108**, 085432 (2023).

[74] S. Vajna, E. Simon, A. Szilva, K. Palotas, B. Ujfalussy, and L. Szunyogh, Higher-order contributions to the Rashba-Bychkov effect with application to the Bi/Ag(111) surface alloy, Phys. Rev. B **85**, 075404 (2012).

[75] M. A. U. Absor and F. Ishii, Doping-induced persistent spin helix with a large spin splitting in monolayer snse, Phys. Rev. B **99**, 075136 (2019).

[76] See Supplemental Material at http://link.aps.org/supplemental/10.1103/PhysRevB.109.115141 for the detailed derivation of the $k \cdot p$ Hamiltonian, fitting calculation of the spin splitting, and the calculation of the Z_2 topological invariant.

[77] M. P. Walser, C. Reichl, W. Wegscheider, and G. Salis, Direct mapping of the formation of a persistent spin helix, Nat. Phys. **8**, 757 (2012).

[78] C. Schönhuber, M. P. Walser, G. Salis, C. Reichl, W. Wegscheider, T. Korn, and C. Schüller, Inelastic light-scattering from spin-density excitations in the regime of the persistent spin helix in a GaAs-AlGaAs quantum well, Phys. Rev. B **89**, 085406 (2014).

[79] P. Chuang, S.-C. Ho, L. W. Smith, F. Sfigakis, M. Pepper, C.-H. Chen, J.-C. Fan, J. P. Griffiths, I. Farrer, H. E. Beere, G. A. C. Jones, D. A. Ritchie, and T.-M. Chen, All-electric all-semiconductor spin field-effect transistors, Nat. Nanotechnol. **10**, 35 (2015).

[80] B. Liang, A. Wang, J. Zhou, S. Ju, J. Chen, K. Watanabe, T. Taniguchi, Y. Shi, and S. Li, Clean BN-encapsulated 2D FETs with lithography-compatible contacts, ACS Appl. Mater. Interfaces **14**, 18697 (2022).

[81] A. I. Dago, Y. K. Ryu, F. J. Palomares, and R. Garcia, Direct patterning of p-type-doped few-layer WSe$_2$ nanoelectronic devices by oxidation scanning probe lithography, ACS Appl. Mater. Interfaces **10**, 40054 (2018).

[82] C. L. Kane and E. J. Mele, Quantum spin Hall effect in graphene, Phys. Rev. Lett. **95**, 226801 (2005).

[83] J. Jia, E. Marcellina, A. Das, M. S. Lodge, B. Wang, D.-Q. Ho, R. Biswas, T. A. Pham, W. Tao, C.-Y. Huang, H. Lin, A. Bansil, S. Mukherjee, and B. Weber, Tuning the many-body interactions in a helical luttinger liquid, Nat. Commun. **13**, 6046 (2022).

[84] T. Fukui and Y. Hatsugai, Quantum spin Hall effect in three dimensional materials: Lattice computation of Z_2 topological invariants and its application to Bi and Sb, J. Phys. Soc. Jpn. **76**, 053702 (2007).

[85] W. Feng, J. Wen, J. Zhou, D. Xiao, and Y. Yao, First-principles calculation of Z_2 topological invariants within the fp-lapw formalism, Comput. Phys. Commun. **183**, 1849 (2012).

[86] H. Sawahata, N. Yamaguchi, and F. Ishii, Electric-field-induced Z_2 topological phase transition in strained single bilayer Bi(111), Appl. Phys. Express **12**, 075009 (2019).

[87] L. Fu and C. L. Kane, Topological insulators with inversion symmetry, Phys. Rev. B **76**, 045302 (2007).

[88] S. Singh, J. Kim, K. M. Rabe, and D. Vanderbilt, Engineering weyl phases and nonlinear Hall effects in T$_d$-MoTe$_2$, Phys. Rev. Lett. **125**, 046402 (2020).

[89] S. Paul, S. Karak, M. Mandal, A. Ram, S. Marik, R. P. Singh, and S. Saha, Tailoring the phase transition and electron-phonon coupling in 1T′-Mote$_2$ by charge doping: A raman study, Phys. Rev. B **102**, 054103 (2020).